



Part-scale thermo-mechanical modelling of distortions in Laser Powder Bed Fusion – Analysis of the sequential flash heating method with experimental validation

Bayat, Mohamad; Klingaa, Christopher G.; Mohanty, Sankhya; De Baere, David; Thorborg, Jesper; Tiedje, Niels S.; Hattel, Jesper H.

Published in:
Additive Manufacturing

Link to article, DOI:
[10.1016/j.addma.2020.101508](https://doi.org/10.1016/j.addma.2020.101508)

Publication date:
2020

Document Version
Publisher's PDF, also known as Version of record

[Link back to DTU Orbit](#)

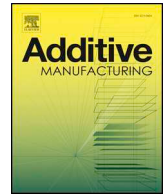
Citation (APA):
Bayat, M., Klingaa, C. G., Mohanty, S., De Baere, D., Thorborg, J., Tiedje, N. S., & Hattel, J. H. (2020). Part-scale thermo-mechanical modelling of distortions in Laser Powder Bed Fusion – Analysis of the sequential flash heating method with experimental validation. *Additive Manufacturing*, 36, Article 101508. <https://doi.org/10.1016/j.addma.2020.101508>

General rights

Copyright and moral rights for the publications made accessible in the public portal are retained by the authors and/or other copyright owners and it is a condition of accessing publications that users recognise and abide by the legal requirements associated with these rights.

- Users may download and print one copy of any publication from the public portal for the purpose of private study or research.
- You may not further distribute the material or use it for any profit-making activity or commercial gain
- You may freely distribute the URL identifying the publication in the public portal

If you believe that this document breaches copyright please contact us providing details, and we will remove access to the work immediately and investigate your claim.



Part-scale thermo-mechanical modelling of distortions in Laser Powder Bed Fusion – Analysis of the sequential flash heating method with experimental validation

Mohamad Bayat*, Christopher G. Klingaa, Sankhya Mohanty, David De Baere, Jesper Thorborg, Niels S. Tiedje, Jesper H. Hattel

Department of Mechanical Engineering, Technical University of Denmark, Building 425, 2800 Kgs. Lyngby, Denmark

ARTICLE INFO

Keywords:

L-PBF
Thermo-mechanical model
Part-scale
Finite element
Ti6Al4V

ABSTRACT

Residual stresses and deflections are two major issues in laser-based powder bed fusion (L-PBF) parts. One of the most efficient and reliable ways for predicting residual stresses and final distortions is via a calibrated numerical model. In this work, a part-scale finite element thermo-mechanical model for Ti6Al4V is developed in the commercial software Abaqus/CAE 2018. The flash heating (FH) method is used as the initial multi-scaling law to avoid time-consuming meso-scale simulations. The model has been verified by doing a mesh-independency analysis. To check the validity of the model, dedicated experiments involving samples with specific scanning strategies were performed. Experimental measurements were made by optical 3D scanning with the fringe projection technique. An in-house made Python script was written for the stripe-wise and layer-wise partitioning of the numerical model, along with material and boundary condition attributions. As expected, the results show that layer-wise FH is insensitive to the scanning pattern and will lead to an isotropic stress field. It is shown that the FH method overestimates the minimum deflection magnitude compared to the experiments by 46.2 %. Sequential FH (SFH) is then proposed to resolve this problem. Results show that by refining the stripe widths in SFH from 15 mm to 1.5 mm, the deviation between the predicted and measured deflection reduces from 35.7 % to 1.19 %. However, the required computational time increases from 9.3 h to 65 h.

1. Introduction

Additive manufacturing (AM), also denoted 3D-printing, is a manufacturing process where components essentially are made by adding material in a layer-by-layer manner. AM has certain advantages as compared to more traditional production methods, mainly due to its unique capability of producing complex assembled geometries as well as having low material waste in addition to short end-to-end manufacturing time [1].

In Laser Powder Bed Fusion (L-PBF), first the powder table moves a small distance in the vertical direction upwards while at the same time the build table moves with the same displacement in the opposite direction. Hereafter, the coating tool moves towards the build table and spreads a layer of fine metallic powder particles. After the powder-laying step, the laser starts scanning the defined areas fed by the input CAD file. The laser intensity is sufficiently high, so that it can easily melt down and fuse the discrete powder particles together. After cooling down, these two steps repeat until the entire part is

manufactured.

Even though L-PBF outperforms conventional production methods such as milling, casting, etc. in certain areas [2], it does indeed not imply that it is a defect-free process, rather on the contrary. Usually there are several types of defects present in L-PBF samples, e.g. lack-of-fusion voids [3], surface waviness [4], keyhole porosity [5] and at a much larger scale residual stresses [6], cracks [7] and unwanted deflections [8]. These defects occur not only at different length-scales but they also originate from different phenomena. In this respect, studying such a complex and transient multi-physics and multi-scale process solely by means of experimental observations is not sufficient. Accordingly, a numerical model that is validated against experimental results can provide a lot of insight into the process and the involved phenomena and their respective physics.

In recent years, a tremendous amount of research has been carried out on modelling of metal AM. The models are typically developed for addressing various objectives such as analyzing heat [9–11] and fluid flow conditions [12,13], porosity formation [14–17], surface [18,19],

* Corresponding author.

E-mail address: mbayat@mek.dtu.dk (M. Bayat).

metallurgical conditions [20,21] and microstructural evolution [22]. In addition to these simulations, Finite Element (FE) models incorporating Computational Solid Mechanics (CSM) have been widely used for thermal and mechanical analysis of the L-PBF process [6,7,23–34].

There are different types of classifications of such thermo-mechanical FE-based models, for example based on scale, type of coupling, material model and multi-scaling rules, etc. From a length-scale point of view, one can divide the existing FE-based models into meso-scale and part-scale, which are sometimes also called macro-scale. In the meso-scale category, typically a fully or sequentially coupled thermo-mechanical model is used. In this group, the effect of the laser beam is usually modelled via a moving concentrated body heat source [26,34]. These models can give a high-resolution stress/strain or thermal field, however, their computational domain is fairly small and is typically less than 1 cm by 1 cm with a few layers of thickness [26,30,32]. Accordingly, almost all of the current meso-scale thermo-mechanical models in literature are used to study small cubic or plate-like geometries [7,25–27,30,32,34]. According to Williams et al. [35] and Ferro et al. [36], these meso-scale models are dedicated to model few tracks and layers due to high computational requirements, since a very fine spatio-temporal resolution is required. As noted by several authors, the meso-scale models cannot be applied to engineering applications, unless a proper multi-scaling or agglomeration technique is implemented [6,23,24,28,29,31].

As a remedy to this problem, several researchers have proposed various multi-scaling laws to enable modelling of thermo-mechanical conditions of real-sized samples at an affordable computational cost. Gouge et al. [31] classified these types of indirect modelling of the L-PBF process into four essentially different groups: Inherent Strain (IS), Agglomerated Laser (AL), Flash Heating (FH) and multi-scaling laws. Each of these approaches has its pros and cons; IS requires either an a-priori and detailed meso-scale thermo-mechanical numerical model [31,37] or experimental data from which the inherent strain can be derived. Furthermore, the IS method will not give any information regarding the thermal conditions during the L-PBF process since it in essence is a static mechanical model. The AL method can, to a large extent, capture the correct thermo-mechanical conditions with a good accuracy, but it requires an astonishing amount of CPU resources [31]. FH [23,38,39] is considered to be a fast-responding thermo-mechanical model that under some certain model conditions (e.g. model layer thickness, contact time, etc.) gives satisfactory stress/strain and thermal fields. This method in its original layer-by-layer form, as will be shown in this work later on, is insensitive to the scanning pattern and consequently leads to unrealistic deflection fields. The last category, the multi-scaling laws, as can also be inferred from their names, require running of three different scales of simulations in tandem, which affects the total computational time significantly, as three models need to be developed and calibrated [8,33,40].

In this work an FE-based part-scale fully coupled thermo-mechanical model of the L-PBF process of the Ti6Al4V alloy is developed. The model can predict the temperature and stress fields during the course of the process. The model also includes the cutting process (from the base-plate) and predicts the final permanent deflection. The model is developed in Abaqus/CAE 2018 and includes temperature-dependent material properties and involves phase change, conduction, radiation and convection heat transfer modes. An in-house made Python script does automatic partitioning of the CAD file and attributes the necessary boundary conditions. The model has been verified and validated via mesh-independency analysis and comparison of the predicted stress field with data in literature. To further validate the developed numerical model, dedicated samples with specific scanning strategies are made. The experimental measurements are made with 3D scanning using the fringe projection technique. The FH method has been used as the initial agglomeration or lumping technique to model the process.

The evolution of the stress field and its distribution during the process is studied. To improve the FH method, the SFH technique is introduced. Detailed comparison between these two techniques, based on the residual stress field, final deflection and the required computational time, is given in the paper as well. Finally, the effect of choosing different stripe sizes on the final deformation of the sample is investigated.

2. Experimental setup and measurements

2.1. Sample

The component investigated in this work is a square plate made of Ti6Al4V and part of a larger build job. The intention of making these parts is to investigate the effect of different laser scanning patterns and island strategies on the final deformation and residual stress. Process steps and the part geometry are shown in Fig. 1(a)–(c) and (d), respectively

Fig. 1(a) shows a snapshot during the L-PBF process. Details of the laser specifications are given in Table 1. Fig. 1(b) shows the final build plate which includes samples and Fig. 1(c) is a snapshot during the Electrical Discharge Machining (EDM) process which was used to detach the samples from the base plate. Fig. 1(d) shows the final part geometry: A square plate with a nominal size of 30 mm by 30 mm by 1 mm is built on the top of 2 mm thick support structure.

The part was made with a uni-directional scanning pattern as shown in Fig. 2. This means that the laser started from one end of the plate and shut off after reaching the other end. After that, the laser moves back to the first end and starts scanning a new line. The hatch distance was 80 μm .

The scanning starts from the bottom right corner in Fig. 2 and continues its way along the x axis. Then it shifts to the next track along the y axis. The sweep direction is the direction in which the sequence of tracks are scanned and this term will be used throughout the paper hereafter. Furthermore, the cutting direction is opposite to the sweep direction, as shown in Fig. 2(a).

2.2. Optical scanning

The titanium plates were scanned using a D800 optical 3D scanning system produced by 3Shape [41]. The software used for the data-acquisition and calibration is the Convince® 2015 Quality Control System (Premium version). This system utilizes the fringe projection technique which allows for the position of the points to be calculated using optical triangulation [42–44]. The triangulation approach is based on a setup consisting of one projector and two cameras. The fringe pattern enables the generation of matching points that are used for triangulation.

Right before the measurements, the scanner was performance verified using a designated 3Shape calibration kit and an automated procedure performed by the software. After calibration, the components were mounted on a polymer brick using an adhesive material. Then the component was scanned using default settings but with manually determined scanning orientations. The sample was scanned from seven different vertical angles and eight evenly distributed horizontal angles at each vertical level, totaling 56 automatic scans.

In the final step an STL file was generated and the file was analyzed using the GOM Inspect software. The warpage analysis was conducted by using the least squares plane method which enables both a quantitative and qualitative evaluation of the warpage of the plates [45]. Finally, a surface distance map was generated by conducting a nominal/actual comparison between the nominal geometry and the STL obtained from the 3D scanning.

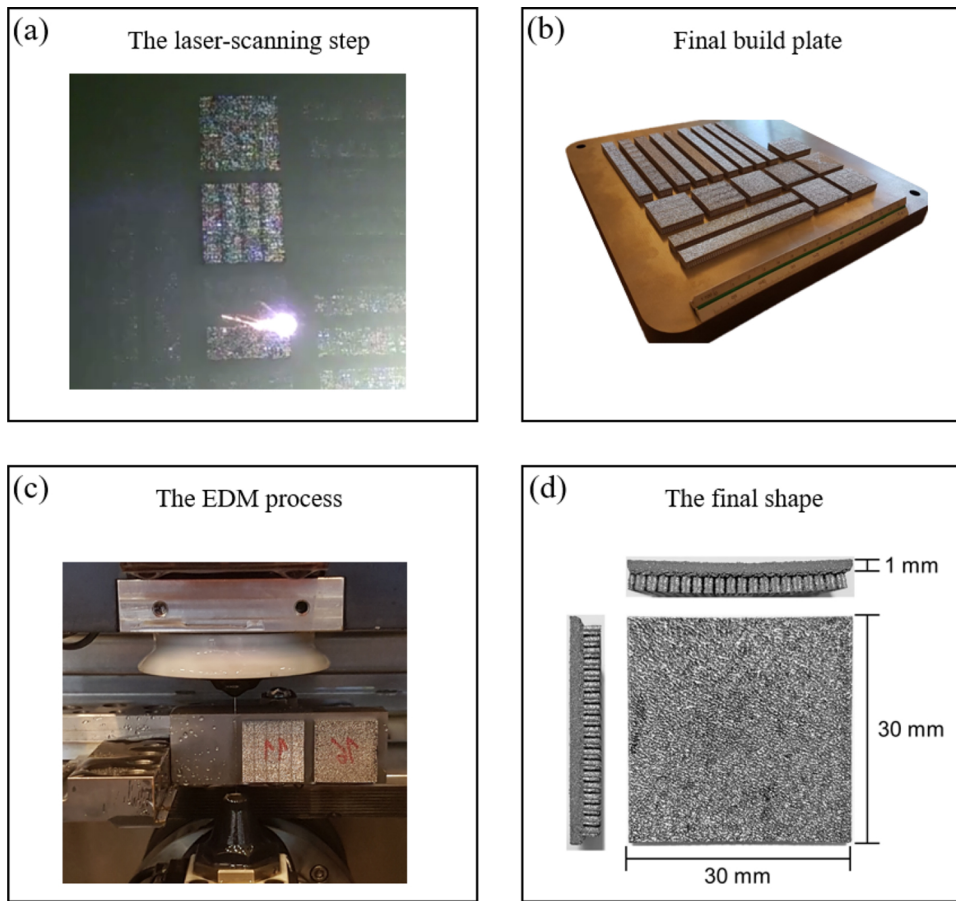


Fig. 1. (a) In-situ image of the process, (b) final build plate configuration, (c) the EDM process and (d) the part dimensions (after cut).

Table 1
Laser specifications and process conditions.

Process parameter	Value
Laser power (P)	120 W
Laser travel speed (v_{laser})	800 mm. s ⁻¹
Effective beam radius (r_b)	40 μ m
Hatch spacing (H)	80 μ m
Powder layer thickness (δ)	50 μ m

3. Numerical model

The well-known partial differential equations expressing energy balance and static force equilibrium are solved to find the temperature and stress/strain/deflection fields, respectively. All material properties are temperature-dependent and in the thermal model, phase change due to melting and solidification is also considered. An in-house made Python code takes the component's CAD file along with the laser specifications (e.g. hatch size, power, absorptivity, the travel speed, etc.) and automatically performs the stripe-wise and layer-wise partitioning

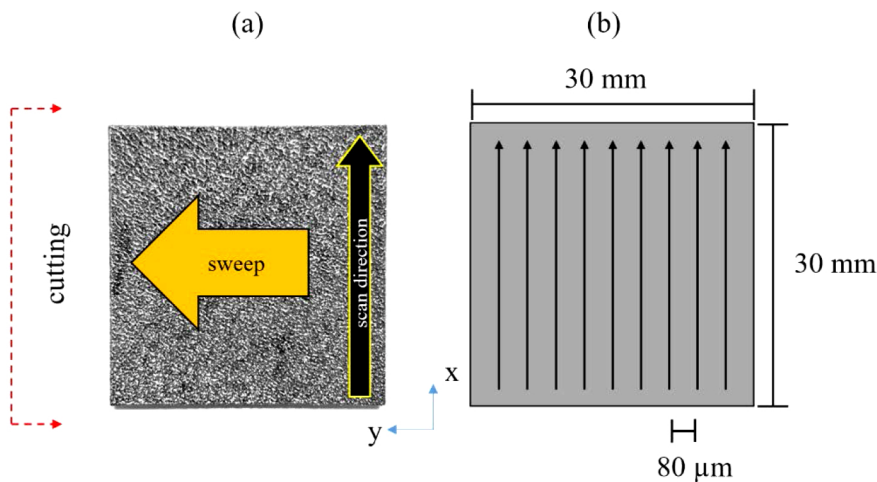


Fig. 2. (a) Sweep and cutting directions for the process. (b) Scanning pattern and hatch sizes. Note that the same coordinate system is also used for the FE model.

along with the needed material model and boundary condition attribution. Element birth and death is implemented to sequentially activate the part components in the SFH method (model change in the software). The model is developed in Abaqus/CAE 2018.

3.1. Heat transfer

The transient heat conduction equation is solved in the computational domain to obtain the temperature field during the course of the process

$$\rho C_p \frac{\partial T}{\partial t} = \frac{\partial}{\partial x} \left(k \frac{\partial T}{\partial x} \right) + \frac{\partial}{\partial y} \left(k \frac{\partial T}{\partial y} \right) + \frac{\partial}{\partial z} \left(k \frac{\partial T}{\partial z} \right) - \rho \cdot \Delta H_{sl} \cdot \frac{\partial f_{liq}}{\partial t} + \dot{Q}_V \quad (1)$$

In Eq. (1), density ρ (kg m^{-3}), specific heat capacity C_p ($\text{J kg}^{-1} \cdot \text{K}^{-1}$) and thermal conductivity k ($\text{W m}^{-1} \cdot \text{K}^{-1}$) are all volume-averaged during the solidification interval [46].

$$k = f_{sol} k_{sol} + f_{liq} k_{liq}, \quad (2)$$

$$C_p = \frac{\rho_{sol} \cdot C_{p,sol} \cdot f_{sol} + \rho_{liq} \cdot C_{p,liq} \cdot f_{liq}}{\rho_{sol} \cdot f_{sol} + \rho_{liq} \cdot f_{liq}}, \quad (3)$$

$$\rho = f_{sol} \cdot \rho_{sol} + f_{liq} \cdot \rho_{liq}. \quad (4)$$

f_{liq} (-) and f_{sol} (-) are the liquid and solid fractions, respectively and they sum up to unity. In this work the liquid fraction is assumed to be a linear function of temperature during the solid-liquid phase transition

$$f_{liq} = \begin{cases} 1 & T \geq T_{liq} \\ \frac{T - T_{sol}}{T_{liq} - T_{sol}} & T_{sol} < T < T_{liq} \\ 0 & T \leq T_{sol} \end{cases} \quad (5)$$

Subscripts O_{sol} and O_{liq} stand for the solidus and liquidus temperatures in Eq. (5). ΔH_{sl} (J kg^{-1}) is the latent heat of fusion and Q_V (W m^{-3}) is the volumetric heat source belonging to the FH and SFH methods in Section 3.3.

3.1.1. Thermal boundary and initial conditions

The thermal boundary conditions are shown in Fig. 3 and as seen, only the top exposed areas of every activated meta-layer are subjected to the radiation and convection boundary conditions.

However, the already built walls, which are adjacent to unmolten powder, are approximated to have an adiabatic condition on the sides for simplicity, since loose powder has very low thermal conductivity. The thermal boundary condition for the surfaces, which are exposed to the ambient is given as

$$-k \frac{\partial T}{\partial z} = h_{amb} [T - T_{amb}] + \epsilon \eta [T^4 - T_{amb}^4]. \quad (6)$$

In eq. (6), h_{amb} ($\text{W m}^{-2} \text{K}^{-1}$), ϵ (-) and η ($\text{W m}^{-2} \text{K}^{-4}$) are ambient convective heat transfer coefficient, surface emissivity and Stefan-Boltzmann constant, respectively. The bottom boundary of the base plate is at a constant temperature of 25 °C. Moreover, the initial temperature is set to 25 °C and uniform.

$$T(x, y, z, t = 0) = 25 \text{ } ^\circ\text{C} \quad (7)$$

$$T(z = 0, t) = 25 \text{ } ^\circ\text{C} \quad (8)$$

3.2. Mechanical model

Static equilibrium in three dimensions along with Hooke's general law are solved in an FE framework to find stress/strain fields and deformation.

$$\sigma_{ij,j} = 0, \quad (9)$$

$$\sigma_{ij} = \frac{E}{1 + \nu} \left[\frac{1}{2} (\delta_{ik} \delta_{jl} + \delta_{il} \delta_{jk}) + \frac{\nu}{1 - 2\nu} \delta_{ij} \delta_{kl} \right] e_{kl}^{el}, \quad (10)$$

where σ_{ij} (Pa) and e_{ij}^{el} (-) are stress and elastic strain tensors in Eqs. (9) and (10). E (Pa) and ν (-) are the elastic Young modulus and Poisson's ratio, respectively. According to standard linear strain decomposition, the total incremental strain tensor is the sum of the elastic (e^{el}), plastic (e^{pl}), thermal (e^{th}) and transformation (e^{tr}) incremental strain tensors [47].

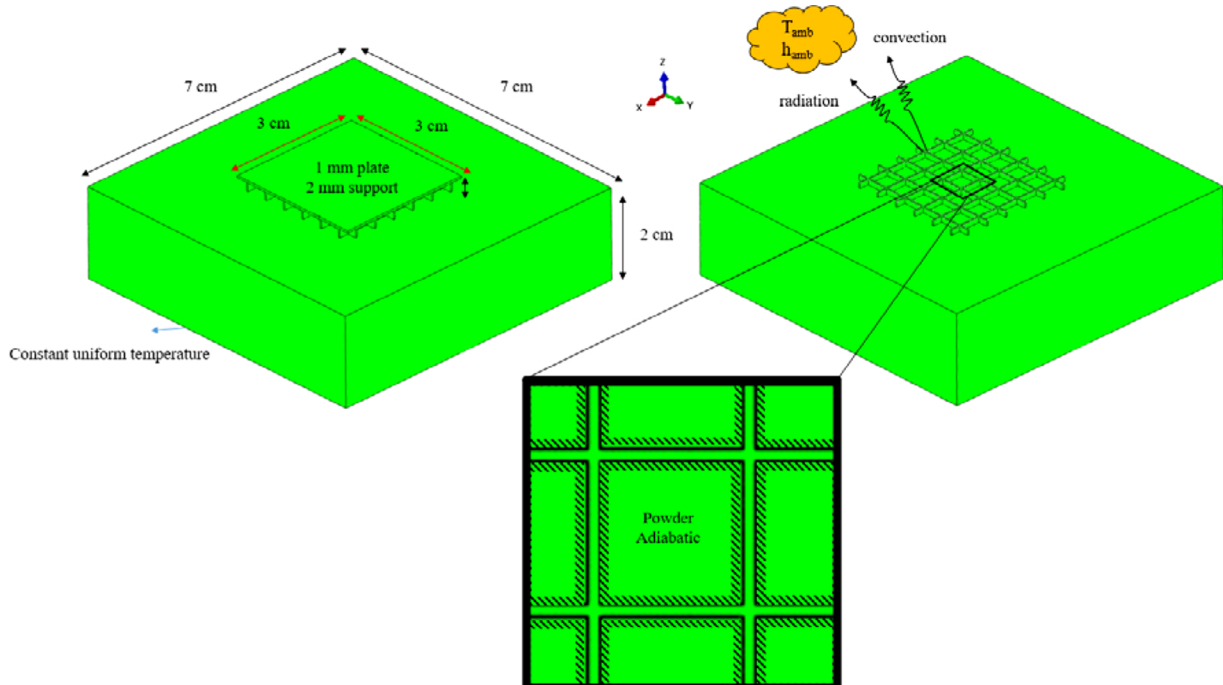


Fig. 3. Model geometry along with the thermal boundary conditions. Note that the walls which are adjacent to un-sintered powder, are approximated to have an adiabatic boundary condition. However, the top surface of the newly deposited layers are exposed to radiation and convection.

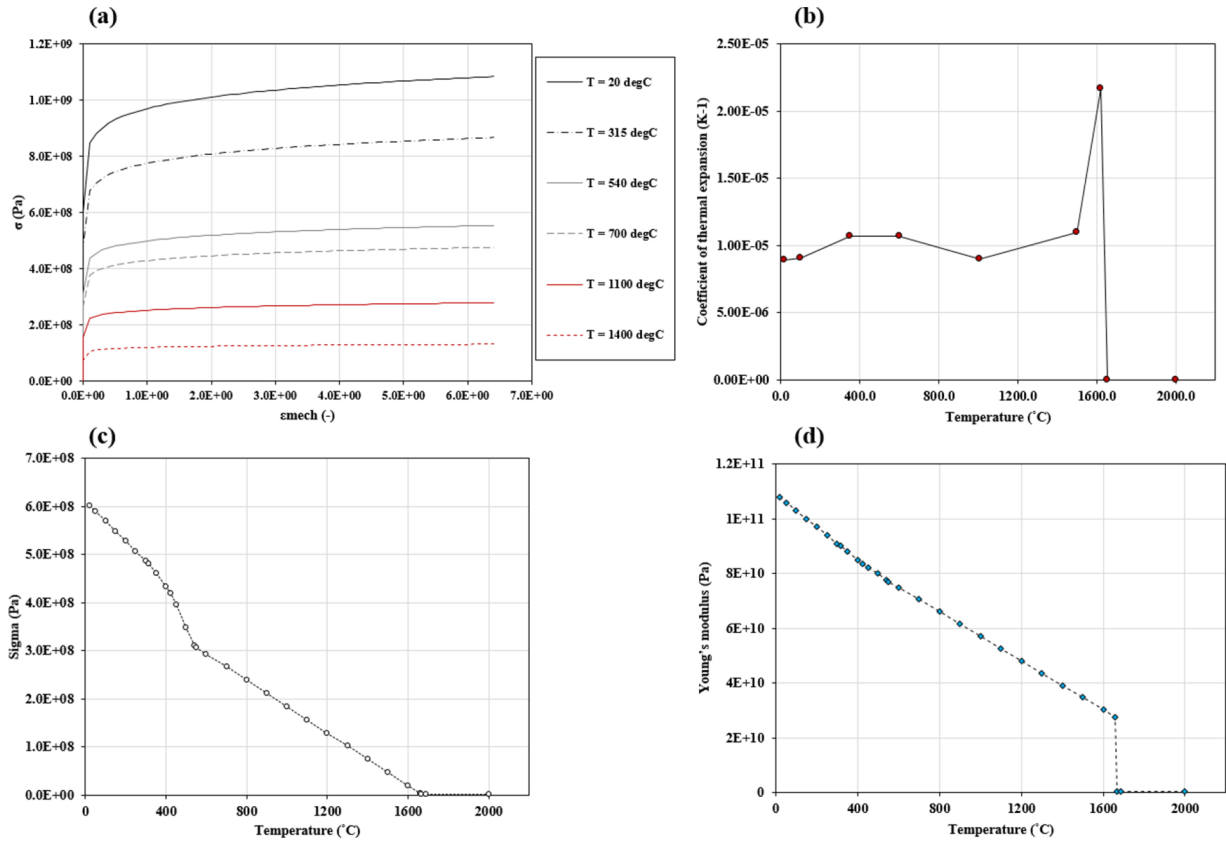


Fig. 4. (a) Yield curves at six different temperatures for Ti6Al4V alloy. The material model is based on power law. (b) The coefficient of thermal expansion as a function of temperature [49]. (c) and (d) respectively show the change in the yield stress and Young's modulus versus temperature.

$$\dot{\epsilon}_{ij}^{total} = \dot{\epsilon}_{ij}^{el} + \dot{\epsilon}_{ij}^{pl} + \dot{\epsilon}_{ij}^{th} + \dot{\epsilon}_{ij}^{tr} = \dot{\epsilon}_{ij}^{mech} + \dot{\epsilon}_{ij}^{th} + \dot{\epsilon}_{ij}^{tr} \quad (11)$$

Even though stress relaxation happens during the process [48], in this work and for simplicity, it is assumed that the transformation strain does not influence the total strain tensor throughout the process, hence it is neglected [7,29,34]. e^{mech} (-) in the above expression is the mechanical strain tensor which is the sum of elastic and plastic strains. According to J2 flow theory, in addition to isotropic hardening,

$$\dot{\epsilon}_{ij}^{pl} = \frac{9}{4} \left[\frac{1}{E_t} - \frac{1}{E} \right] \frac{s_{kl} \dot{\sigma}_{kl}}{\sigma_e^2} s_{ij}. \quad (12)$$

E_t (Pa) is the tangent modulus, σ_e (Pa) is the Von Mises stress and s_{ij} (Pa) is deviatoric stress tensor in Eq. (12). Moreover, the thermal strain is given by

$$e_{ij}^{th} = \alpha(T) \delta_{ij} (T - T_{ref}). \quad (13)$$

α (K⁻¹) is the coefficient of thermal expansion and δ_{ij} is Kronecker delta in Eq. (13). Furthermore, the temperature-dependent material model follows a power-law hardening curve given by

$$e^{mech} = \frac{\sigma}{E} \quad \sigma \leq \sigma_{yield}$$

$$e^{mech} = \frac{\sigma_{yield}}{E} \left[\frac{1}{n} \left(\frac{\sigma}{\sigma_{yield}} \right)^n - \frac{1}{n} + 1 \right] \quad \sigma > \sigma_{yield} \quad (14)$$

where yield stress σ_{yield} (Pa), Young's modulus E (Pa) and power law index n (-) are all functions of temperature in eq. (14). The yield curve and the coefficient of thermal expansion for Ti6Al4V and at a number of different temperatures are shown in Fig. 4(a) and (b), respectively.

Fig. 4(c) and (d) respectively show the yield stress and Young's modulus as a function of temperature.

3.2.1. Mechanical boundary condition and the cutting process

The bottom side of the base plate is set to a pinned boundary condition as shown in Fig. 5. Upon the cutting process, the base plate is deactivated, while the plate remains active with the boundary conditions shown in Fig. 5.

The cutting occurs towards the negative y direction. To obtain the final shape of the sample after the cutting process, a static step is defined. In the static step the sample should be statically determined, hence the two boundary conditions, shown in Fig. 5 are applied. The two points shown in red are on the line which is cut at the final step of the cutting process. The related thermo-physical properties for the model are given in Table 2.

3.3. The FH and SFH methods

In the FH method, instead of resolving the meso-scale laser-material interaction, an equivalent heat source is applied uniformly to the recently activated meta-layer [39]. Some details of this method are given in Fig. 6. Chiumenti et al. [52] used a similar version of FH but with elongated exposure time for the heat source for their purely thermal model.

The total amount of energy transferred by the laser during the scan of an actual layer (the layer's input energy or U_{δ}) is calculated by multiplying the effective laser input power by the layer sweep time t_f (s)

$$U_{\delta} = \xi \cdot P \cdot t_f, \quad (15)$$

where t_f (s) is given by

$$t_f = \frac{A_{\Omega}}{H \cdot v_{laser}}. \quad (16)$$

The laser power and its absorptivity are denoted P (w) and ξ (-) in Eq. (15), respectively. t_f (s) is the total amount of time required to scan

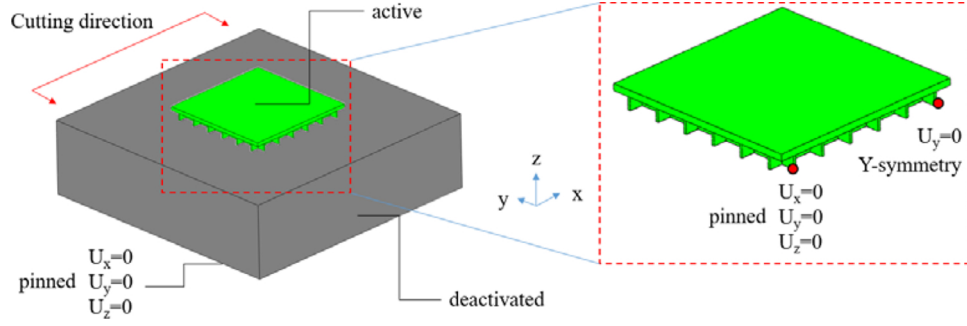


Fig. 5. (left) Cutting step and deactivation of base plate. (right) Imposed boundary conditions on the part + support assembly during the cutting step.

Table 2

Thermo-physical properties of the Ti6Al4V alloy [21,50,51].

Property	Definition	Value	Property	Definition	Value
k_{sol} (W m ⁻¹ K ⁻¹)	Solid thermal conductivity	13	ΔH_{sl} (J kg ⁻¹)	Latent heat of fusion	286000
k_{liq} (W m ⁻¹ K ⁻¹)	Liquid thermal conductivity	33	T_{sol} (K)	Solidus temperature	1893.2
$C_{p,sol}$ (J kg ⁻¹ K ⁻¹)	Solid specific heat capacity	543	T_{liq} (K)	Liquidus temperature	1927.2
$C_{p,liq}$ (J kg ⁻¹ K ⁻¹)	Liquid specific heat capacity	750	h_{amb} (W m ⁻² K ⁻¹)	Ambient coefficient of heat transfer	20

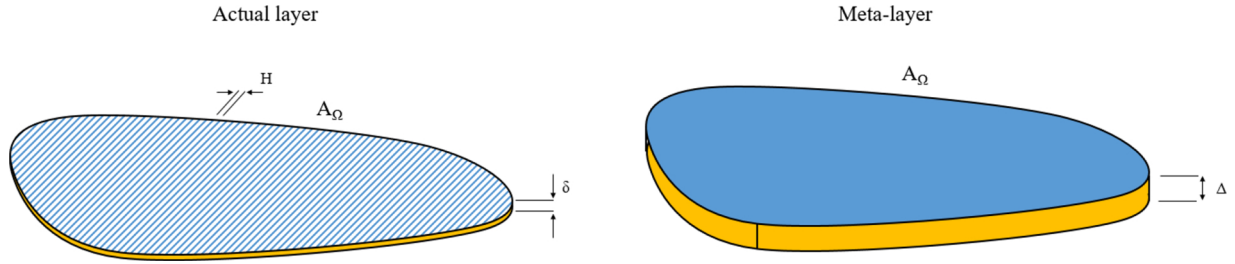


Fig. 6. (Left) Actual layer (with thickness δ) and (right) meta-layer (with thickness Δ). H is the hatch distance.

one actual layer. A_{Ω} (m²) is the top surface area of the layer and H (m) is the hatch distance in Eq. (16). Then agglomeration is carried out by lumping a number of actual layers (with a thickness of δ each) into a single meta-layer (with the thickness of Δ), according to Fig. 6. The meta-layer input energy (U_{Δ}) is determined by

$$U_{\Delta} = U_{\delta} \cdot \left(\frac{\Delta}{\delta} \right), \quad (17)$$

where Δ (m), according to Fig. 6, is the meta-layer thickness, while δ (m) stands for the real layer thickness. To find the required volumetric heat source for the FH method, the meta-layer input energy, expressed in Eq. (17) is divided by the meta-layer's total volume and the contact time as

$$\dot{Q}_v''' = \frac{U_{\Delta}}{\Delta t_{contact} \cdot V_{ML}}, \quad (18)$$

where V_{ML} (m³) is the volume of the meta-layer and $\Delta t_{contact}$ (s) is the FH contact or exposure time, which in this work is assumed to be 5e-4 s. According to a recent work, this parameter has the lowest effect on the stress/strain fields if it is below 2.0 ms [39]. By inserting the meta-layer's volume into Eq. (18) and combining with Eqs. (15)–(17), one obtains

$$\dot{Q}_v''' = \frac{U_{\Delta}}{\Delta t_{contact} \cdot [(A_{\Omega}) \cdot \Delta]} = \frac{\left(\xi \cdot P \cdot \left[\frac{A_{\Omega}}{H \cdot v_{laser}} \right] \right) \cdot \left(\frac{\Delta}{\delta} \right)}{\Delta t_{contact} \cdot [(A_{\Omega}) \cdot \Delta]}, \quad (19)$$

which can be reduced to the following expression for the required volumetric heat source

$$\dot{Q}_v''' = \frac{\xi \cdot P}{H \cdot v_{laser} \cdot \Delta t_{contact} \cdot \delta}. \quad (20)$$

According to Eq. (20), the volumetric heat source required for the FH method is inversely proportional to hatch spacing H (m) and actual layer thickness δ (m).

3.3.1. Time-consistent activation method

A schematic of the activation strategy for FH and SFH is shown in Fig. 7. In the original FH method, the step time equals the total sweep time (t_f) given in Fig. 7 plus the cooling time ($t_f + t_{cool}$). In the SFH method, the step time for each activated stripe is the layer sweep time t_f (s) divided by number of stripes N_s . However, the final stripe of a meta-layer has a longer step time of $t_f / N_s + t_{cool}$ since cooling occurs at the end of the production of every meta-layer. In this way it is assured that the total time for each calculation remains the same (which is $t_f + t_{cool}$), regardless of the choice of stripe width H_{ML} (m). It should be mentioned that the heat source exposure time ($\Delta t_{contact}$) remains unchanged for any FH and SFH case in this work. Furthermore, once implemented, FH or SFH satisfy two essential criteria, first the total amount of energy transferred equals the one in the actual process (as also ensured in Eqs. (15)–(20)) and secondly the total melted zone is the same as in the real process. In other words, the second constraint suggests that there will not remain any unmelted regions during FH or SFH. This will be discussed in the thermal analysis later in the paper.

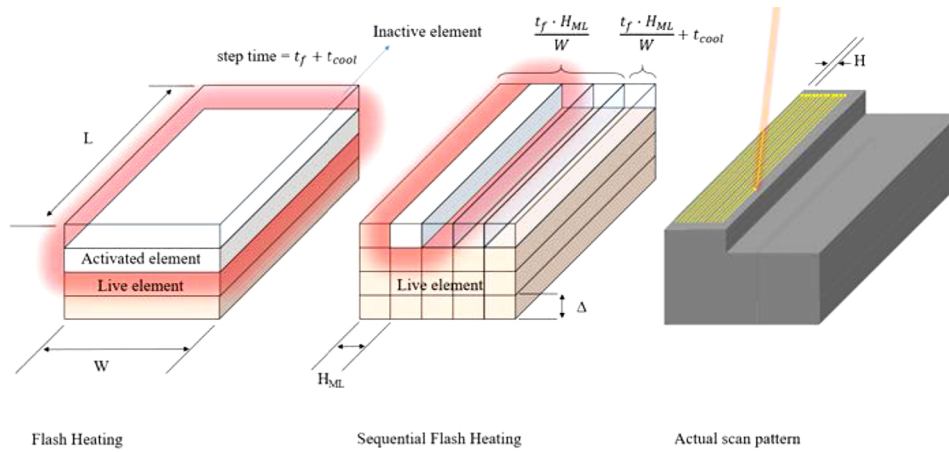


Fig. 7. Step time and activation strategy in the FH and SFH methods. H is the hatch spacing in the actual process and H_{ML} is the model hatch size which in this work is referred as stripe.

4. Results and discussion

Six different cases involving FH and SFH have been modelled in this work. Details of the models e.g. stripe width, case ID, etc. are given in Table 3. The number after SFH denotes the stripe width.

4.1. Validation of the internal stress field

The model has been implemented to simulate the development of the residual stresses in an L-shape component made of 316-L stainless steel. Details of the geometry and the process conditions are given in [28,53]. The sample has a height of 30 mm and according to [53], a laser power of 400 W and a scanning speed $1800 \text{ mm}\cdot\text{s}^{-1}$ are used. The contour of the normal component of the residual stress σ_{33} at the center of the component is shown for both the numerical model (using FH) and

the experiments (using Neutron Diffraction (ND)) in Fig. 8.

According to Fig. 8(a), the numerical model predicts two compression zones inside the two arms of the component. The predicted maximum and minimum σ_{33} stresses are 612.7 MPa and -435.5 MPa, respectively. This leads to about 18 % and 9 % error in the prediction of maximum and minimum σ_{33} stress magnitudes, compared to the experiments. According to Fig. 8(a), a tensile residual stress is predicted on the outer rim of the geometry, see Fig. 8(a). In the numerical model, this very high tensile stress region is clearly observed on the outer rim, while in the experimental image, only the edges possess very high tensile stress. This can be due to the low resolution of the experimental measurements. Moreover, the comparison between Fig. 8(a) and (b) reveals that the developed thermo-mechanical model can predict the residual stresses with a good accuracy. The FH method with 1 mm thick meta-layers has been used for this validation of the model.

Table 3

The model specifications for the FH and SFH approaches. Note that the step time in this table does not mention the 10 s of cooling per each meta-layer. The number after SFH denotes the stripe width.

Approach	Model ID	Stripe size (mm)	Meta-layer thickness (m)	Flash exposure time (s)	Total meta-layer time	Step time (s) – per stripe
FH	SFH-30	30.0	500e-6	2.5e-4	24.0625	14.0625
SFH	SFH-15	15.0				7.0313
	SFH-06	6.0				2.8125
	SFH-03	3.0				1.4063
	SFH-1.5	1.5				0.7031

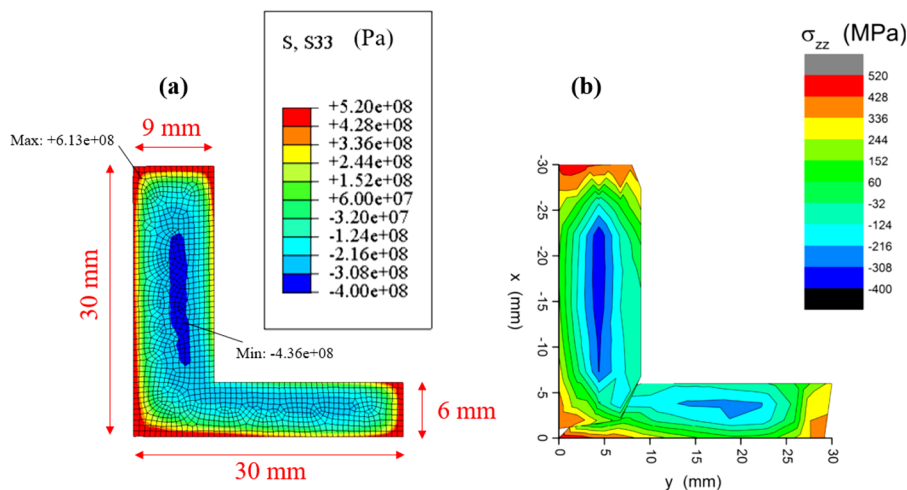


Fig. 8. Contour of σ_{33} stress component at $z = 15 \text{ mm}$: (a) numerical model using FH and (b) experimental data found via ND [28,53].

4.2. Mesh independency check

In order to verify the developed numerical model, a mesh independency analysis has been carried out on the plate. In this respect, three mesh configurations were used to run the FH (SFH-30) case in Table 3. Details of the three models along with the required CPU times are given in Table 4.

The contour of the final (after cutting) vertical deflection field is depicted in Fig. 9 for all three mesh configurations given in Table 4. The contours in Fig. 9(a)–(c) show that the deflection field will not change by refining the mesh from about 45,000 elements to 320,000 elements, while the CPU time increases from 4.87–207 h. Thus, the mesh configuration belonging to medium case in Table 4 is used for modelling the thermo-mechanical conditions for the rest of the paper. The calculations are all done on 20-core cluster machines with Intel® Xeon® W-2195 CPU 2.30 GHz and 256 GB RAM at DTU.

4.3. The FH approach (SFH-30)

The temperature contour at four different stages during the activation of the meta-layers is shown in Fig. 10(a) and (b) respectively show the temperature contours for the first and fourth meta-layers (meta-layers 1–4 belong to the support structures). It is observed that one obtains a uniform peak temperature of about 2200 °C within each meta-layer and this increases only slightly over time from meta-layer to meta-layer. To illustrate the cooling patterns, temperature contours for the fifth meta-layer are shown in Fig. 10(c)–(d) at two different instances of time.

Based on Fig. 10, there are some specific zones of the recently deposited meta-layer that have a temperature lower than the solidus temperature of Ti6Al4V. As time elapses, these areas become even colder and one can visually observe a pattern in the temperature contour, see Fig. 10(c). Based on the blow-up image in Fig. 10, at 1.916 s, it is clearly observed that the regions which are deposited on the support structures cool down at a faster rate than the places where powder with high thermal resistance exists underneath.

Fig. 11(a) shows the temperature profile captured on the top of the

final meta-layer and at the center of the sample along the y axis. The plate is uniformly heated up to about 2200 °C after 1.6 ms of the activation of the final meta-layer. Fig. 11(b) shows the corresponding longitudinal stress profile on the A-A line. According to Fig. 11(b), at $t = 1.6$ ms, the stress state is in compression although having a very small magnitude, since the material is molten and essentially cannot withstand stresses due to almost immediate yielding. At 0.6 s, where the temperature just goes below the solidus line, the stress mode inverts to tension. This is mainly due to the cool down mechanism, where the recent layer cools down at a faster rate than the previous layers and the new layer cannot shrink freely and hence builds up tensile stress [54]. At 1.2 s, the line is completely in the solid state and one can see the effect of supports on the T-y profile in Fig. 11(a). At this time the stress starts to build up in tension, until it reaches an approximate value of 600 MPa, which will be the residual stress for that layer due to the building process. This residual stress is the main factor affecting the final deformation pattern after the cutting process.

Fig. 12(a) and (b) respectively show the contour of the longitudinal and transverse normal components of the stress tensor (σ_{11} and σ_{22}) at the end of the production of the part, right before the cutting step.

A comparison between Fig. 12(a) and (b) reveals that there is no difference between the distribution of the longitudinal and transverse normal stresses, except that they are rotated 90°. Moreover, one can see the effect of these two stresses on the overall Mises stress shown in Fig. 12(c), where accordingly, the edges carry the lowest level of stresses. It is noted that the support structures are subject to a different type of stress state depending on their orientation. It is observed that the support structures, which are oriented along the x-axis, have significant longitudinal stress in tension. The features of the supports, which are elongated along the y axis have a high level of transverse stress, see Fig. 12(d) and (e). The same observation was also reported for a directed energy deposition of metal in [55]. The vertical stress component is shown in Fig. 12(f) at the end of the process. Based on this figure, one can recognize that the outer rim of the support is under tensile vertical stresses, while the inner part is in compression mode. A similar observation was also noticed earlier for an L-shaped sample made of 316 L stainless steel in the validation section. In this situation

Table 4
Details of the mesh configuration for the mesh-independency analysis.

Case	Model ID	Element type	Node count	Element count	CPU time (hrs)
Very fine	FH (SFH-30)	Combined C3D8T and C3D6T	388720	319852	207
Fine			150336	119520	41.3
Medium			61210	45674	4.87

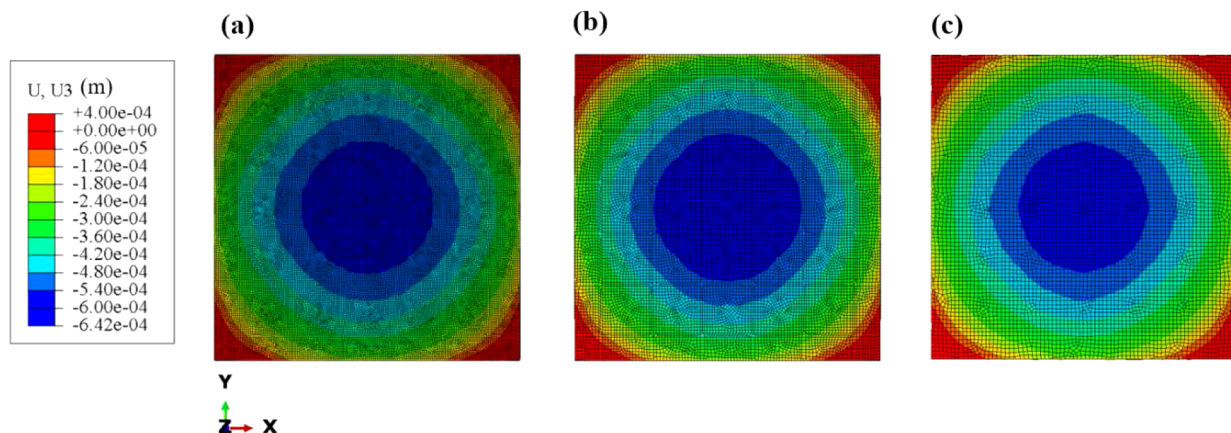


Fig. 9. The contour of final vertical deflection for the FH case for the mesh-independency analysis. (a) Very fine (319852 elements), (b) fine (119520 elements) and (c) medium (45674 elements) mesh configuration.

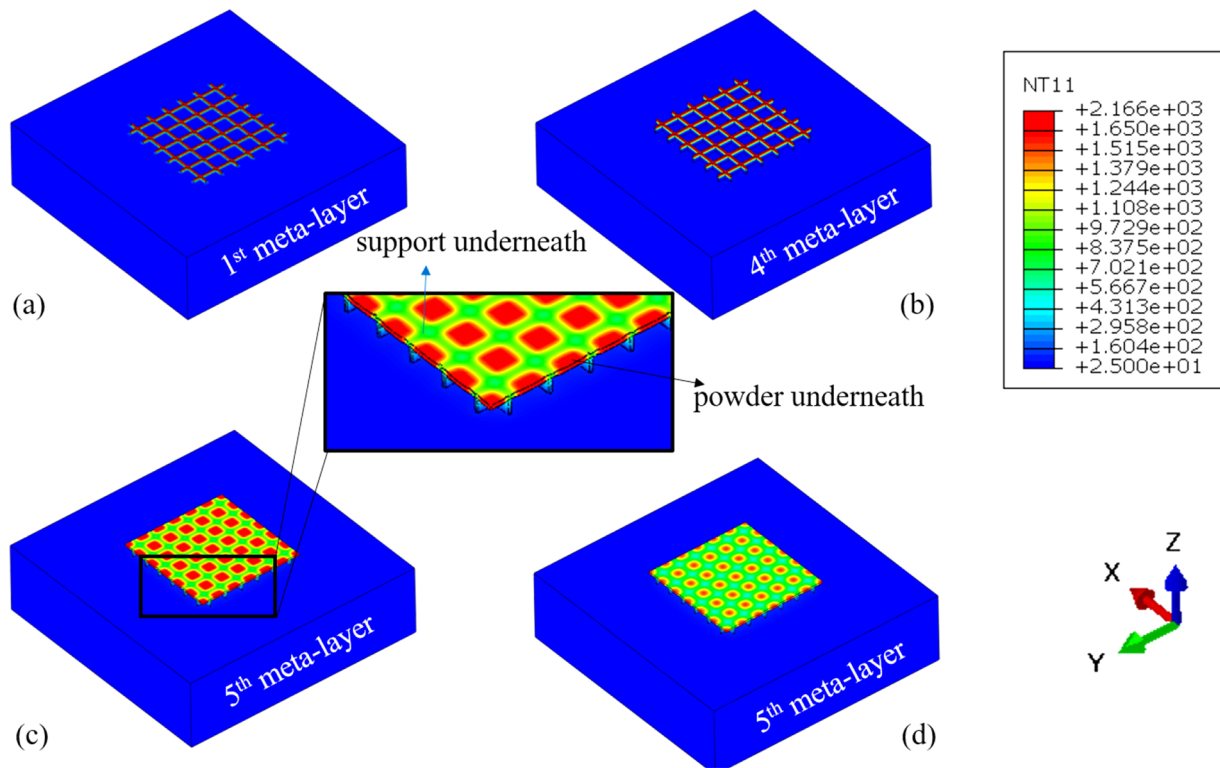


Fig. 10. Temperature contour at $t = 1.6$ ms after the activation of the (a) 1st and (b) 4th meta-layer for the FH method. (c) and (d) show the temperature at $t = 1.916$ s and $t = 2.86$ s for the 5th meta-layer. The temperature unit is degrees Celsius.

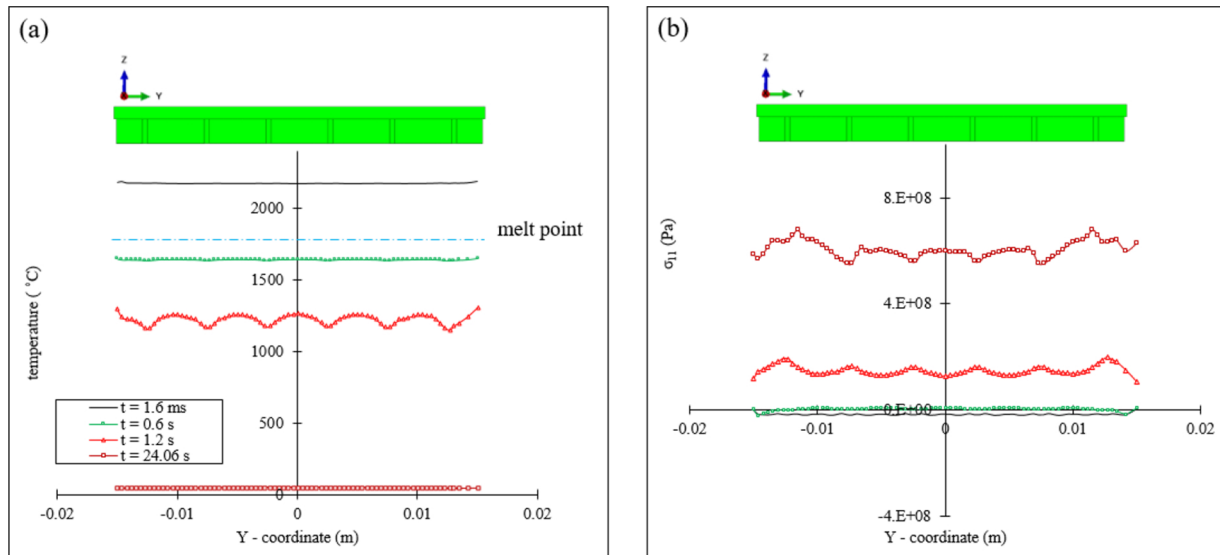


Fig. 11. (left) The temperature profile and (right) the longitudinal stress component at the top center of the plate and along y axis at different instances in time. The legend applies for both figures and the plots are made at end of the process (before cutting).

where the recent layers are in tension mode (in x-y plane), they try to pull the outer rim of the component upwards, hence in this way a tensile vertical stress is induced on the outer rims. To satisfy the z-direction force equilibrium, the central region undergoes compression mode in the vertical stress component; see Fig. 12(f).

4.4. The FH approach

4.4.1. The SFH-15 case

Based on the discussion given above and according to Fig. 12, the σ_{11} and σ_{22} stress components look similar when rotating 90 degrees in

the x-y plane. As expected, this stress state will lead to a fully symmetrical deflection field after the cutting process is completed (see Fig. 9). In this respect, SFH with different stripe (model hatch) sizes was performed with the specifications given in Table 3. As the first case for the SFH approach and according to Table 3, each meta-layer is divided into 2 stripes. The temperature contour at some stages of the laser-scanning step is shown in Fig. 13(a)–(f).

The activation strategy of the model stripes is shown in Fig. 13(a) and (b). The activation is implemented in such a way that the thermal effects of the model are as close as possible to the real case. In the experiments, the laser travels in a uni-directional manner along the x

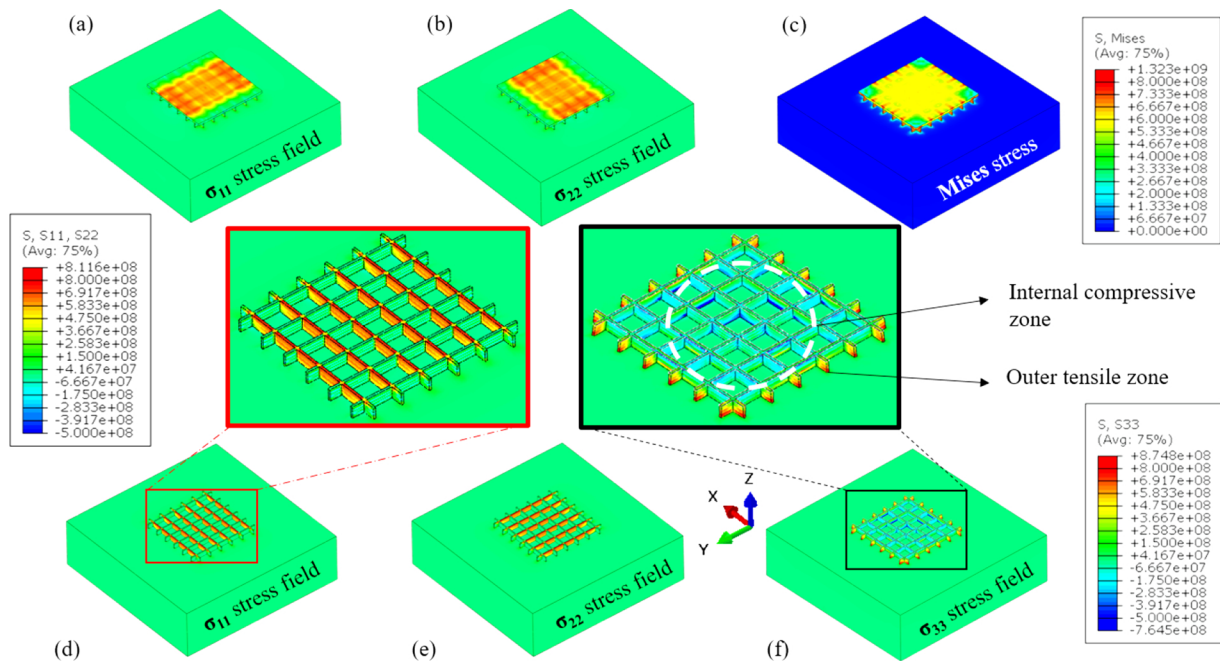


Fig. 12. (a), (d) The longitudinal stress at the end of 6th and 4th meta-layers. (b), (e) The transverse stress at the end of 6th and 4th meta-layers. (c) The Mises stress at the end of the 6th meta-layer. (f) The cut view of the vertical normal stress component tensor (σ_{33}) at the end of the process in the support. The stress units are Pa.

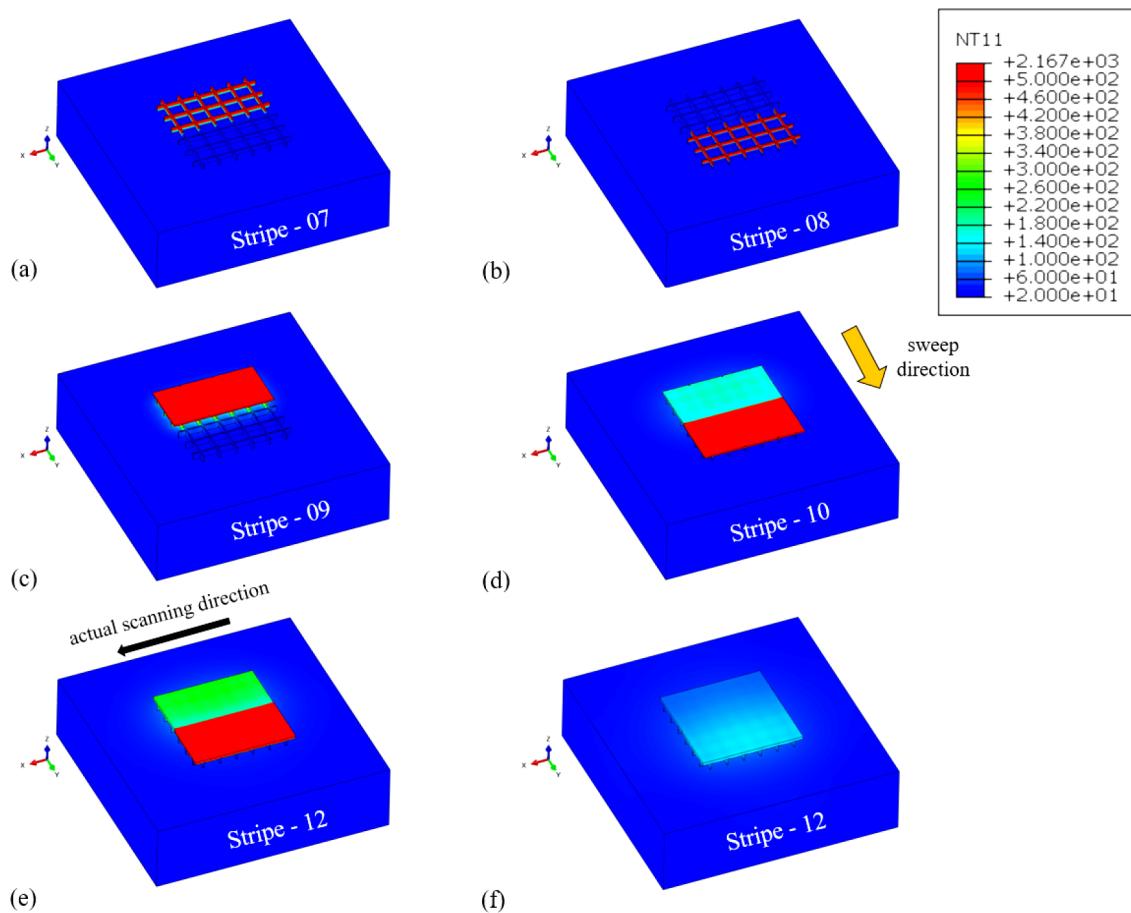


Fig. 13. Temperature contour of the SFH-15 case at the beginning of the activation of : (a) stripe #7, (b) stripe #8, (c) stripe #9, (d) stripe #10, (e) stripe #12. (f) Belongs to stripe #12 and at $t = 17.36$ s. Note that the actual laser pattern and the model sweep direction that resembles the total laser movement in the real process. Units are degrees Celsius.

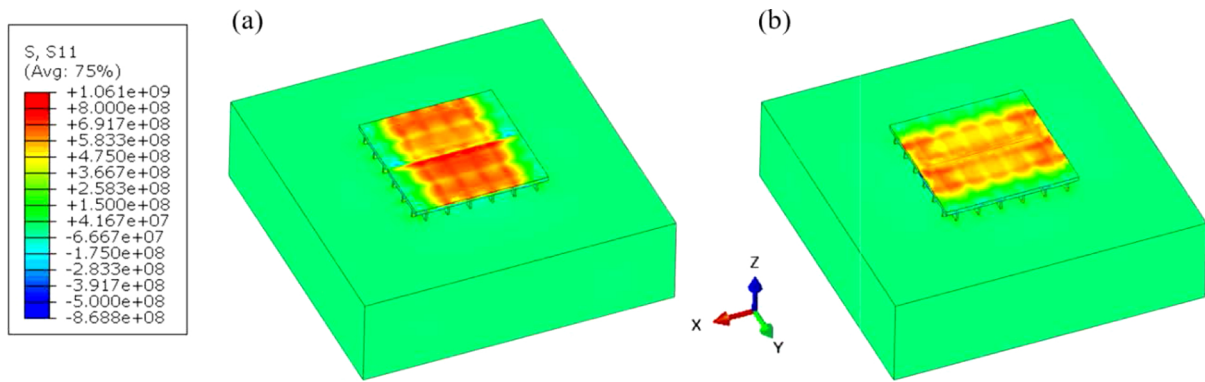


Fig. 14. (a) The longitudinal and (b) transverse stress components at the end of the production of the sample. Units are Pa.

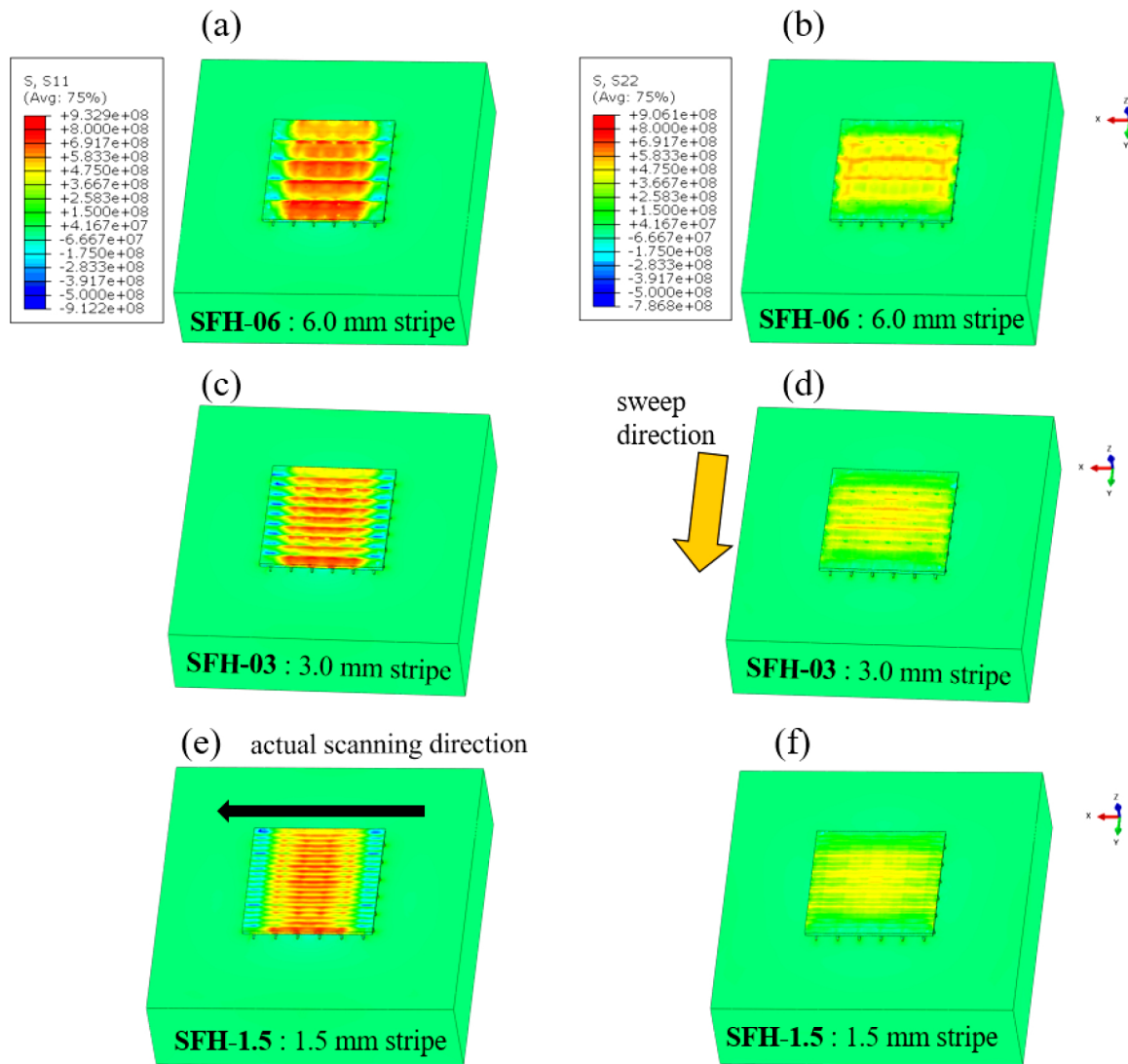


Fig. 15. (left) The longitudinal and (right) the transverse stress contour at the end of the laser-scanning step. (a,b) SFH-06, (c,d) SFH-03 and (e,f) represents SFH-1.5. Stress units are Pa.

coordinate and sweeps towards the y-axis. The model resembles the sweep direction via the activation pattern shown in Fig. 13. According to Fig. 13(a)–(e), which belong to the very beginning of their corresponding steps, the temperature exceeds the solidus temperature all over the strip over the whole thickness of a meta-layer. Furthermore, it is noticed that at $t = 17.36$, the temperature is almost $100\text{ }^\circ\text{C}$, while the step ends at $t = 24.06$ s, see Fig. 13(f). Accordingly, the temperature at

the end of the activation of the final meta-layer approaches the room temperature.

Fig. 14(a) and (b) respectively depict the σ_{11} and σ_{22} stress components at the end of the production of the sample for SFH-15. According to Fig. 14(a) and (b), the planar stresses are no longer identical when rotated 90 degrees as was the case for the FH method in Fig. 12(a) and (b). However, a relatively higher tensile stress is predicted for the

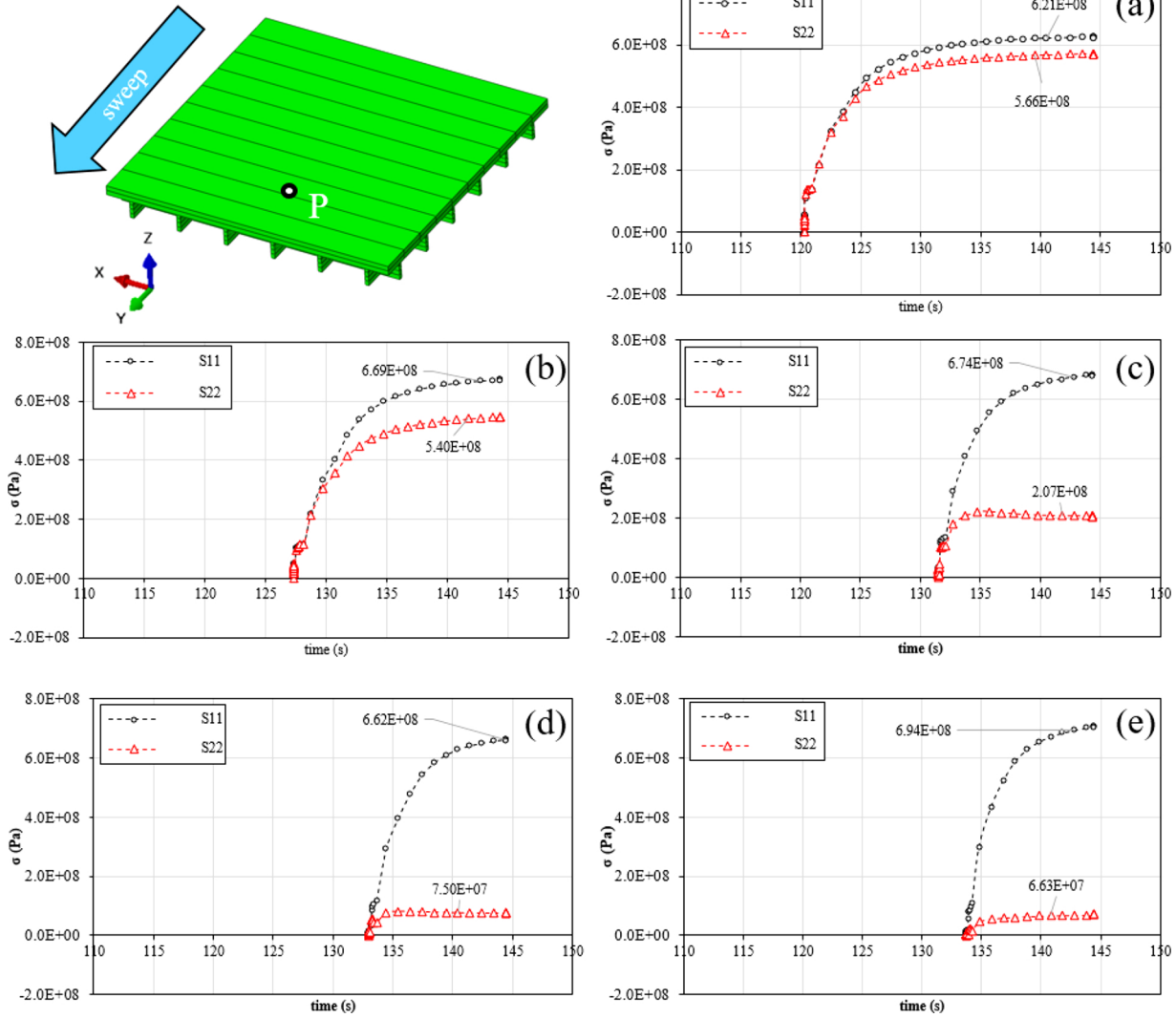


Fig. 16. Top left is the partitioned geometry for case SFH-03 with 3.0 mm stripe width. (a)–(e) are the temporal variation of σ_{11} and σ_{22} versus time at node "P" for SFH-30 – SFH-1.5 cases. The units for the contour are Pa.

longitudinal component, see Fig. 14(a).

4.4.2. Finer stripes: SFH-06, SFH-03 and SFH-1.5

According to Table 3, three more cases have been considered and modelled with finer stripe widths of 6 mm, 3 mm and 1.5 mm. Fig. 15(a)–(f) show the longitudinal and transverse normal stress components at the end of the production of the plate. The stress level in SFH-06 is much higher in the longitudinal direction than the transverse direction, according to Fig. 15 (a) and (b).

According to Fig. 15 and by dividing the plates into more finer stripes, σ_{11} and σ_{22} will no longer be identical as seen in Fig. 12 for the FH method (SFH-30). According to Fig. 15, by choosing finer stripe widths, a continuous and tensile residual stress field will form in the longitudinal direction. This observation is in line with meso-scale thermo-mechanical models where the laser movement was resolved by a moving heat source [30,32,56]. To have a more quantitative understanding of this anisotropy in the planar stress state, an investigation point called "P" has been put at a fixed location on the top of the final meta-layer, see Fig. 16.

According to Fig. 16(a), both the σ_{11} and σ_{22} components of stress, increase in tension mode until they both reach a magnitude of about 600 MPa. Accordingly, σ_{11} and σ_{22} are very close in their final magnitude for the original layer-by-layer FH method. However, as can be

observed in Fig. 16(b) and (c), dividing the meta-layer into more stripes, will lead to different growth rates for σ_{11} and σ_{22} . It is noted that that the longitudinal stress remains almost in the same level as predicted for the SFH-30 case, however, the transverse stress becomes much lower with finer stripe widths. This trend is also observed in Fig. 16(d) and (e), where the stripes have a width of 3.0 mm and 1.5 mm, respectively. Furthermore, it seems that further reducing the stripe width from 3.0 mm to 1.5 mm will not affect the σ_{22} level significantly, as seen in Fig. 16(d) and (e). This means that by reducing the stripe width, an anisotropy in the planar stress field will form, mainly because of lowering of σ_{22} , according to Fig. 16. In other words, one can mend the unphysical isotropic stress field arising from the layer-by-layer FH method by making activation in a stripe-wise-layer-wise manner, rather than only in a layer-wise way.

4.4.3. Thermal conditions - The SFH method

In the actual L-PBF process, usually a laser with a beam size of less than 100 μm starts scanning the sample with a speed of 500–1000 $\text{mm}\cdot\text{s}^{-1}$, depending on the machine [57]. Recent high-fidelity numerical models with the inclusion of fluid dynamics show a concentrated temperature field around the laser position [21]. However, the SFH method cannot resolve such a detailed transient temperature field. Temperature contours for four cases of SFH-15 to SFH-

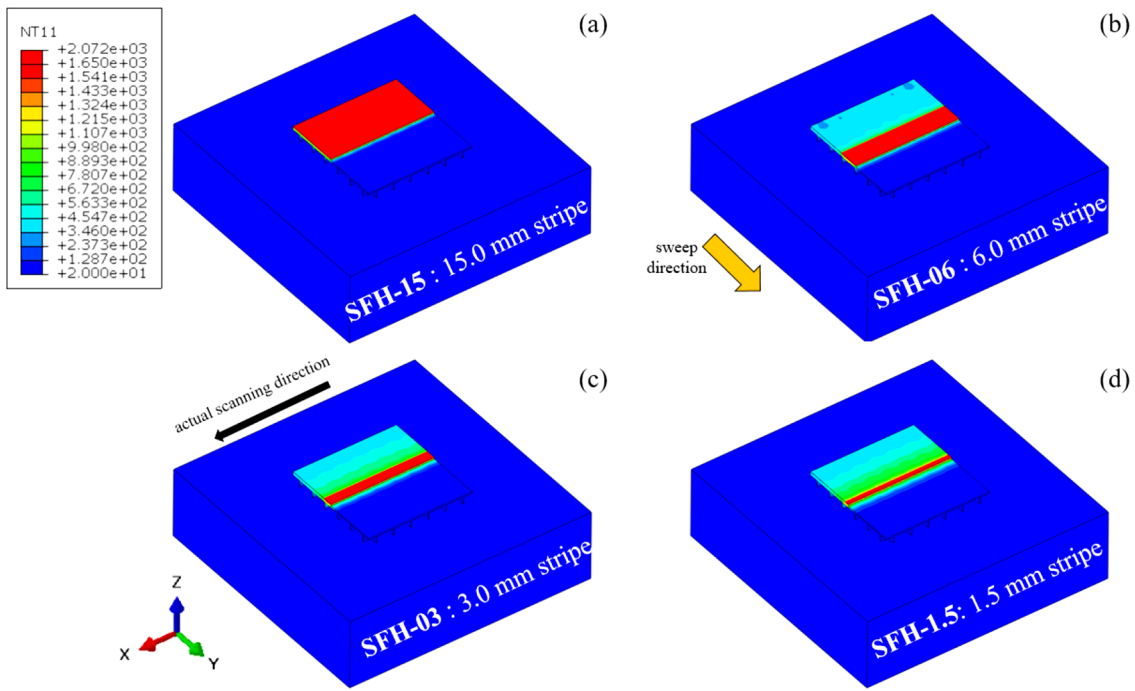


Fig. 17. The temperature contour at a time instance where laser reaches approximately the center of the final meta-layer for (a) SFH-15, (b) SFH-06, (c) SFH-03 and (d) SFH-1.5. Units are degrees Celsius.

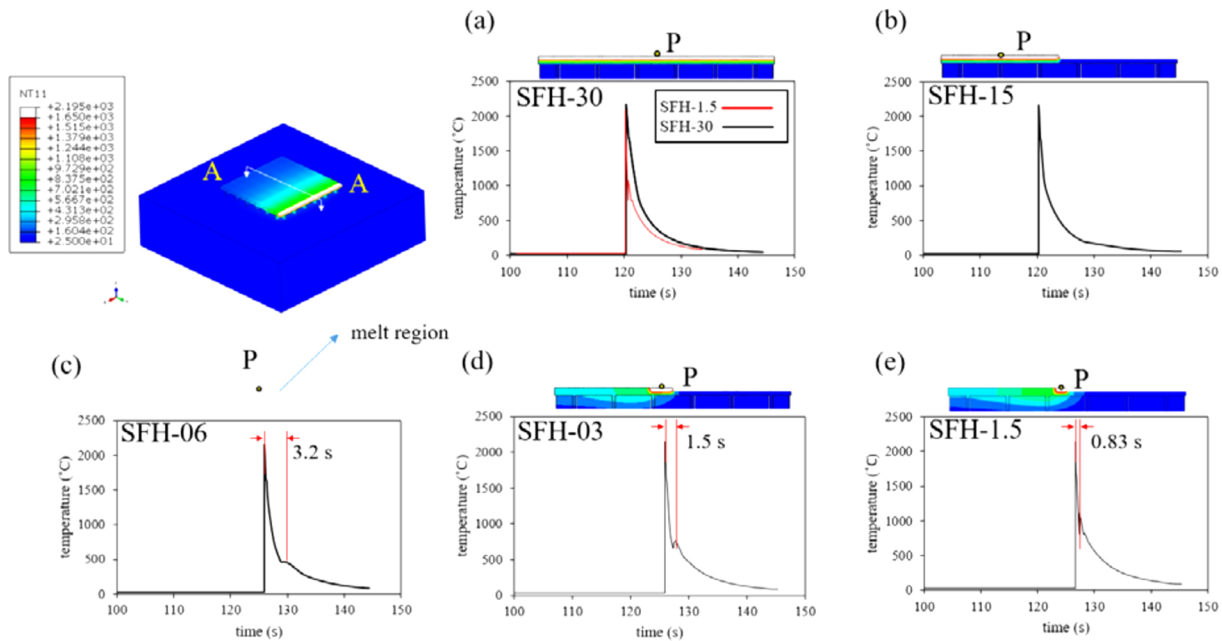


Fig. 18. Top left is the temperature contour for SFH-1.5. White color for all contours shows the regions of which are above liquid temperature. (a)-(e) show the temperature-time profile captured at their corresponding nodal probe "P". Note that the position of the investigation point is not the same for all cases.

1.5 (arising from the SFH method) are depicted in Fig. 17 at the time instance where the laser would have reached the center of the final powder layer. The algorithm written in the previously mentioned Python script is developed in such a way that the temperature field and the total input energy have the highest resemblance to the actual thermal field where a concentrated laser beam scans the powder layer. For instance, the time at which a new stripe is being activated and exposed to the heat source is identical for all SFH-15 to SFH-1.5 cases and matches with the real process.

For the SFH-15 case in Fig. 17(a), even though the total energy input and total fused volume matches with the real case, the

temperature field is far from reality, as artificially half of the final meta-layer is above the melting point. Reducing the stripe width to 6 mm in the SFH-06 case leads to a more non-uniform thermal field. For SFH-02 and SFH-1.5, the model can better capture the local heating due to the moving laser. However, obviously the method cannot predict the non-uniformity in the temperature field due to the laser movement along the x direction. Moreover, it should be mentioned that the SFH approach can be used to model the thermo-mechanical conditions in the L-PBF process with continuous island scanning strategies. In this way the stripe width should equal the island width and the sweep direction can be defined to model the process.

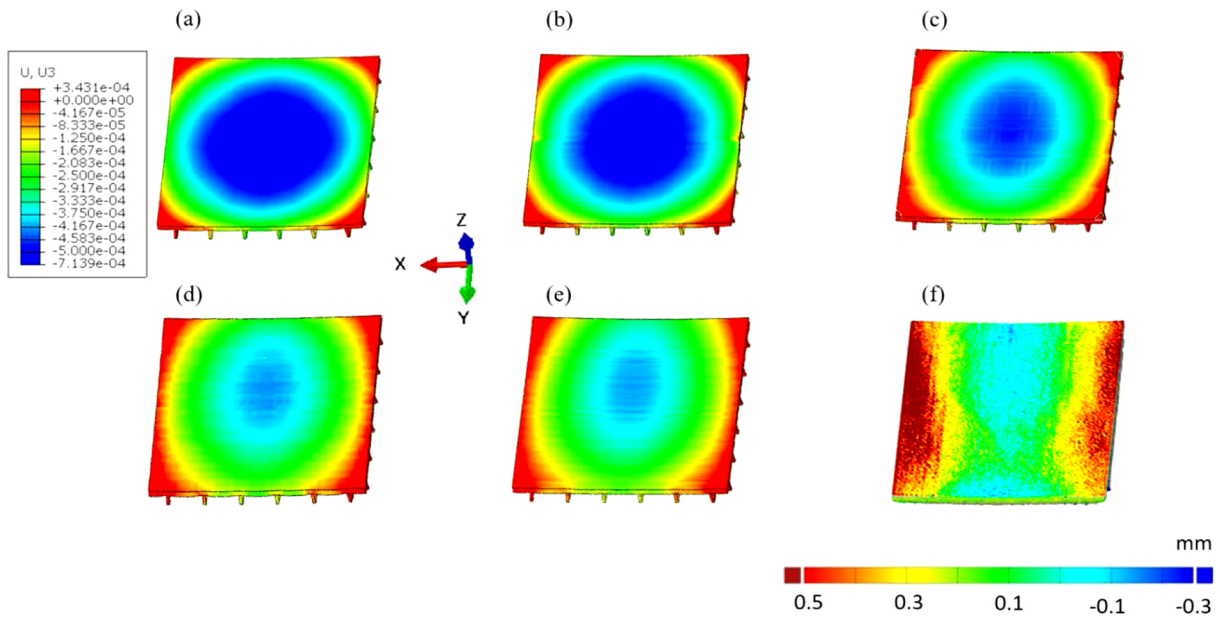


Fig. 19. Final z-deflection field after the cutting process for: (a) SFH-30, (b) SFH-15, (c) SFH-06, (d) SFH-03 and (e) SFH-1.5. (f) is the actual measurements done by 3D scanning with the fringe projection technique.

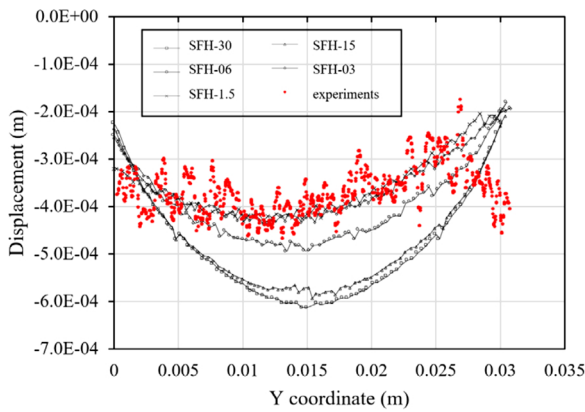


Fig. 20. Plot of final deflected shape against y coordinate at the center of the plates. Red dots show the experimental data points (For interpretation of the references to colour in this figure legend, the reader is referred to the web version of this article).

Table 5
Numerical and experimental data and the required CPU hours for each model.

Case ID	Numerical (m)	Experiments (m)	Deviation (%)	CPU time (hrs)
FH (SFH-30)	-6.14E-04	-4.20E-04	-46.19	4.87
SFH-15	-5.70E-04		-35.71	9.32
SFH-06	-4.95E-04		-17.86	23.57
SFH-03	-4.36E-04		-3.81	41.56
SFH-1.5	-4.15E-04		1.19	65.24

Fig. 18 shows a cross-sectional view of the SFH-30 to SFH-1.5 cases at the time where they have reached their corresponding maximum temperature. The regions which are heated above this melting point are colored in white in Fig. 18. In addition to the temperature contours, Fig. 18(a)–(e) show plots of temperature versus time captured by a set of point probes. These probes were set at the center of one recently activated stripe belonging to cases SFH-30 to SFH-1.5. Their place is shown in Fig. 18(a)–(e) with the point denoted “P”.

Regardless of the stripe sizes, the maximum temperature is found to

be almost the same for all cases, according to Fig. 18(a)–(e). The maximum temperature based on Fig. 18 has a value around 2200 °C. According to Fig. 18(a) and (b), the temperature probes show a sharp heating curve which is followed by a cooling that starts right after the exposure time. The two curves shown in Fig. 18(a) and (b) look similar, except after 130 s where a very small increase in temperature is noticed in the SFH-15 case, see Fig. 18(b). This second peak, however negligible, is due to the activation of the second stripe which activates approximately 7 s later.

Further refinement of the stripes to 6 mm in case SFH-06 (see Fig. 18(c)) will lead to a clear appearance of two peaks. For the SFH-06 case, the second peak occurs in about 3.2 s after the activation of this stripe. In SFH-03 an even sharper second peak of about 700 °C happens within an even shorter time of 1.5 s after the first peak, see Fig. 18(d). Finally for SFH-1.5, where the stripe is 1.5 mm wide, the second peak goes up to around 1000 °C and takes place 0.83 s after the first peak. These thermal cycling periods and peaks will have a significant effect on the metallurgical conditions in the adjacent solidified tracks.

By superimposing the temperature-time curve derived from SFH-1.5 on SFH-30, an interesting information is obtained, see Fig. 18(a). According to this figure, even though there is a second heating due to the following activated stripe for SFH-1.5, the material cools down at a faster rate in SFH-1.5 as compared to SFH-30. The underlying reason can be explained by the fact that the cooling rate is proportional to the area/volume ratio of a stripe. This ratio is proportional to L^{-1} and L is the characteristic length. Choosing a smaller stripe leads to bigger value of L^{-1} and hence a higher cooling rate is predicted. This means that smaller stripe widths will cause higher cooling rates. The solidification cooling rate for SFH-1.5 is about -2771 K s^{-1} while it is -855 K s^{-1} for H-01, which once more underlines the effect of stripe width on cooling rate.

4.4.4. Final deflection: SFH vs FH

Finally, the methodology proposed in Section 3.3 for modelling of the cutting process was performed on cases SFH-30 to SFH-1.5. The final deflection field for all five cases in addition to the actual measurements done by 3D-scanning are shown in Fig. 19.

According to Fig. 19(a), the deflection field is symmetrical and the sample has bent upwards especially at the corners and to a lesser extent at the edges. Furthermore, a big zone of negative deflection in the

center is predicted for SFH-30 in Fig. 19(a). This deflection field is formed directly because of the isotropic stress field in the X-Y plane, shown earlier. However, by dividing the meta-layers into 2 stripes, the deflection field is no longer symmetrical, see Fig. 19(b). It is also noted that by further reducing the stripe widths, the zone with negative deflection will shift upwards and along the negative y axis, according to Fig. 19(c)–(e). The numerical model measures the deflection with respect to the undeformed geometry, while the surface deviation color map is made by comparing the derived CAD file with a plane which passes directly into the center of mass of the U-shape profile of the plate. To have a quantitative comparison, the final deflected profile of the plate is plotted against the y coordinate in Fig. 20, for all cases along with the experimental data points at the center of the plates.

According to Figs. 19 and 20, one can see that the model can better predict the deflection field, if finer stripes are used. Furthermore, by coarsening the stripes, the location of the minimum deflection shifts towards the center of the plate, see Fig. 20. There is a mismatch observed at $y = 0.03$ m in Fig. 20 between the predicted and measured deflection profiles. This can be due to the thermal effects during the EDM cutting that might have affected the plate's profile, as the heat transfer is ignored in the cutting step in the model. Based on Fig. 19(d) and (e), and Fig. 20, further refinement of the stripes from 3.0 mm to 1.5 mm, will not affect the final deflection field significantly. By dividing the part into finer stripes, a strong and continuous tensile stress field forms in the longitudinal direction which warps the sample in the x direction. However, as noted earlier, the transverse normal stress is neither high enough nor sufficiently continuous in the y-direction to be able to bend the sample significantly in the y direction as was the case for the standard FH method. Table 5 lists the minimum deflections found from the numerical simulations and their deviation from the experimental data. The latter is the minimum point of the averaged curve-fit going through the experimental data points.

According to Table 5, the FH method predicts a minimum deflection of -6.14×10^{-4} m, which is 46.2 % more (in magnitude) than the corresponding experimental value. Also, in Table 5, it is noticed that the deviation decreases by refining the stripe size. The last two cases, SFH-03 and SFH-1.5, have a deviation of 3.81 % and 1.19 %, respectively. However, the computational cost increases significantly when a finer stripe size is used. According to Table 5, the FH case requires about 5 h of runtime, while the SFH-1.5 required 65 h, which is about 13 times more than that of the FH case. The trend in Table 5 shows that the accuracy will not significantly change, if a finer stripe size than 3.00 mm is going to be used, however, the computational cost will increase to a large extent. Compared to the SFH technique, the inherent strain technique is shown to be able to predict the final deformation of industrial samples at a far lower computational time of less than one hour [58]. However, the inherent strain method will not give any information about the thermal conditions during the process and as mentioned earlier, the calculation of inherent strain component requires an additional numerical or experimental analysis as well.

The samples in this work were manufactured using optimized process conditions for manufacturing while using different scanning strategies. The grid thickness was approximately 400 μ m. However, it was noticed that some of the specimens broke at some specific zones upon cutting, when the island scanning strategies were used. These samples neatly broke along the islands' perimeter. This can perhaps be due to lack of overlap between the islands or due to the support structure as a relatively large inter-wall gap of about 5 mm was used.

5. Conclusion

In this work a part-scale finite element thermo-mechanical model is developed for the L-PBF process of Ti6Al4V material. The thermal model includes phase change, conduction, convection and radiation heat transfer modes. The model is fully coupled and is developed in the commercial software Abaqus/CAE 2018. An in-house made Python

script is developed which does the stripe-wise and layer-wise partitioning on the CAD file, based on the input laser and powder layer information. Material attribution along with imposing proper boundary and initial conditions are also carried out with this Python script. Flash Heating (FH) is used as the multi-scaling approach to avoid fine meso-scale simulations which require unacceptable amounts of CPU resources. The model has been verified and validated through mesh-independency analysis and comparison with experimental results in literature. To further validate the model, dedicated experiments are carried out through the production of samples with specific scanning strategies. Experimental measurements are made by 3D scanning with the fringe projection technique.

Results show that the FH method will lead to an isotropic residual stress field which causes a symmetrical deflection field after the cutting process. As expected, this confirms that FH is insensitive to the scanning pattern or even to the scanning sequence. Results show that the FH method overestimates the minimum deflection magnitude by 46.2 %. As a remedy to this problem, the Sequential Flash Heating (SFH) method is proposed where the activation procedure is treated in a stripe-wise-layer-wise manner. Results show that by refining the stripe widths until a certain level, not only the isotropic stress field vanishes, but also the final deflection field gets much closer to the experimental measurements. According to the results, by choosing a stripe size of respectively 3.0 mm and 1.5 mm (opposed to 30 mm in FH), the error reduces to 3.81 % and 1.19 % in predicting the minimum deflection. In this way and by choosing narrower stripes, a continuous and much higher stress field forms in the longitudinal direction (parallel to the laser pass) compared to the transverse direction in which the transverse stress field is relaxed due to the loss of connectivity. However, it must be underlined that the computational time required for the case with 1.5 mm stripe width is 65 h compared to the 4.87 h required for FH.

CRedit authorship contribution statement

Mohamad Bayat: Conceptualization, Investigation, Formal analysis, Visualization, Methodology, Validation, Writing - original draft. **Christopher G. Klingaa:** Investigation, Formal analysis, Writing - original draft. **Sankhya Mohanty:** Writing - review & editing. **David De Baere:** Writing - review & editing. **Jesper Thorborg:** Conceptualization, Supervision, Resources, Writing - review & editing. **Niels S. Tiedje:** Writing - review & editing. **Jesper H. Hattel:** Conceptualization, Supervision, Funding acquisition, Resources, Writing - review & editing.

Declaration of Competing Interest

The authors have no conflicts of interest to declare.

Acknowledgments

This work has received funding from the European Union Horizon 2020 Marie Skłodowska-Curie ITN PAM² project under grant agreement number [721383] which is highly acknowledged.

References

- [1] Q. Shi, D. Gu, M. Xia, S. Cao, T. Rong, Effects of laser processing parameters on thermal behavior and melting/solidification mechanism during selective laser melting of TiC/Inconel 718 composites, *Opt. Laser Technol.* 84 (2016) 9–22.
- [2] N. Hopkinson, R. Hague, P. Dickens, *Rapid Manufacturing: an Industrial Revolution for the Digital Age*, John Wiley & Sons, 2020.
- [3] N.T. Aboulkhair, N.M. Everitt, I. Ashcroft, C. Tuck, Reducing porosity in AlSi10Mg parts processed by selective laser melting, *Addit. Manuf.* 1 (2014) 77–86.
- [4] G. Yu, D. Gu, D. Dai, M. Xia, C. Ma, Q. Shi, On the role of processing parameters in thermal behavior, surface morphology and accuracy during laser 3D printing of aluminum alloy, *J. Phys. D Appl. Phys.* 49 (13) (2016).
- [5] W.E. King, et al., Observation of keyhole-mode laser melting in laser powder-bed fusion additive manufacturing, *J. Mater. Process. Technol.* 214 (12) (2014)

- 2915–2925.
- [6] J.L. Bartlett, X. Li, An overview of residual stresses in metal powder bed fusion, *Addit. Manuf.* 27 (January) (2019) 131–149.
 - [7] L. Parry, I.A. Ashcroft, R.D. Wildman, Understanding the effect of laser scan strategy on residual stress in selective laser melting through thermo-mechanical simulation, *Addit. Manuf.* 12 (2016) 1–15.
 - [8] C. Li, J.F. Liu, X.Y. Fang, Y.B. Guo, Efficient predictive model of part distortion and residual stress in selective laser melting, *Addit. Manuf.* 17 (2017) 157–168.
 - [9] Y. Huang, L.J. Yang, X.Z. Du, Y.P. Yang, Finite element analysis of thermal behavior of metal powder during selective laser melting, *Int. J. Therm. Sci.* 104 (2016) 146–157.
 - [10] A. Foroozmehr, M. Badrossamay, E. Foroozmehr, S. Golabi, Finite Element Simulation of Selective Laser Melting process considering Optical Penetration Depth of laser in powder bed, *Mater. Des.* 89 (2016) 255–263.
 - [11] L. Ladani, J. Romano, W. Brindley, S. Burlatsky, Effective liquid conductivity for improved simulation of thermal transport in laser beam melting powder bed technology, *Addit. Manuf.* 14 (2017) 13–23.
 - [12] Y.S. Lee, W. Zhang, Modeling of heat transfer, fluid flow and solidification microstructure of nickel-base superalloy fabricated by laser powder bed fusion, *Addit. Manuf.* 12 (2016) 178–188.
 - [13] Effects of sulfur concentration and Marangoni convection on melt-pool formation in transition mode of selective laser melting process, *Mater. Des.* 179 (2019) 107866.
 - [14] M. Bayat, et al., Keyhole-induced porosities in Laser-based Powder Bed Fusion (L-PBF) of Ti6Al4V: high-fidelity modelling and experimental validation, *Addit. Manuf.* (August) (2019) 100835.
 - [15] M. Bayat, S. Mohanty, J.H. Hattel, Multiphysics modelling of lack-of-fusion voids formation and evolution in IN718 made by multi-track/multi-layer L-PBF, *Int. J. Heat Mass Transf.* 139 (2019) 95–114.
 - [16] C. Tang, J.L. Tan, C.H. Wong, A numerical investigation on the physical mechanisms of single track defects in selective laser melting, *Int. J. Heat Mass Transf.* 126 (2018) 957–968.
 - [17] M. Zheng, et al., A novel method for the molten pool and porosity formation modelling in selective laser melting, *Int. J. Heat Mass Transf.* 140 (2019) 1091–1105.
 - [18] C. Qiu, C. Panwisawas, M. Ward, H.C. Basoalto, J.W. Brooks, M.M. Attallah, On the role of melt flow into the surface structure and porosity development during selective laser melting, *Acta Mater.* 96 (2015) 72–79.
 - [19] H. Wang, Y. Zou, Microscale interaction between laser and metal powder in powder-bed additive manufacturing: conduction mode versus keyhole mode, *Int. J. Heat Mass Transf.* 142 (2019) 118473.
 - [20] Z. Gan, H. Liu, S. Li, X. He, G. Yu, Modeling of thermal behavior and mass transport in multi-layer laser additive manufacturing of Ni-based alloy on cast iron, *Int. J. Heat Mass Transf.* 111 (2017) 709–722.
 - [21] M. Bayat, S. Mohanty, J.H. Hattel, A systematic investigation of the effects of process parameters on heat and fluid flow and metallurgical conditions during laser-based powder bed fusion of Ti6Al4V alloy, *Int. J. Heat Mass Transf.* 139 (2019) 213–230.
 - [22] Y. Zhang, J. Zhang, Modeling of solidification microstructure evolution in laser powder bed fusion fabricated 316L stainless steel using combined computational fluid dynamics and cellular automata, *Addit. Manuf.* 28 (July) (2019) 750–765 2018.
 - [23] M.F. Zaeh, G. Branner, Investigations on residual stresses and deformations in selective laser melting, *Prod. Eng.* 4 (1) (2010) 35–45.
 - [24] M. Chiumenti, et al., Numerical modelling and experimental validation in Selective Laser Melting, *Addit. Manuf.* 18 (2017) 171–185.
 - [25] P. Tan, F. Shen, B. Li, K. Zhou, A thermo-metallurgical-mechanical model for selective laser melting of Ti6Al4V, *Mater. Des.* 168 (2019) 107642.
 - [26] Y. Li, K. Zhou, P. Tan, S.B. Tor, C.K. Chua, K.F. Leong, Modeling temperature and residual stress fields in selective laser melting, *Int. J. Mech. Sci.* 136 (December) (2018) 24–35 2017.
 - [27] N.E. Hodge, R.M. Ferencz, J.M. Solberg, Implementation of a thermomechanical model for the simulation of selective laser melting, *Comput. Mech.* 54 (1) (2014) 33–51.
 - [28] N.E. Hodge, R.M. Ferencz, R.M. Vignes, Experimental comparison of residual stresses for a thermomechanical model for the simulation of selective laser melting, *Addit. Manuf.* 12 (2016) 159–168.
 - [29] R.K. Ganeriwala, et al., Evaluation of a thermomechanical model for prediction of residual stress during laser powder bed fusion of Ti-6Al-4V, *Addit. Manuf.* 27 (March) (2019) 489–502.
 - [30] E.R. Denlinger, Thermomechanical model development and in situ experimental validation of the laser powder-bed fusion process, *Thermo-Mechanical Model. Addit. Manuf.* 16 (2017) 215–227.
 - [31] M. Gouge, E. Denlinger, J. Irwin, C. Li, P. Michaleris, Experimental validation of thermo-mechanical part-scale modeling for laser powder bed fusion processes, *Addit. Manuf.* 29 (December) (2019) 100771 2018.
 - [32] B. Cheng, S. Shrestha, K. Chou, Stress and deformation evaluations of scanning strategy effect in selective laser melting, *Addit. Manuf.* 12 (2016) 240–251.
 - [33] C. Li, Y. Guo, X. Fang, F. Fang, A scalable predictive model and validation for residual stress and distortion in selective laser melting, *CIRP Ann.* 67 (1) (2018) 249–252.
 - [34] C. Chen, J. Yin, H. Zhu, Z. Xiao, L. Zhang, X. Zeng, Effect of overlap rate and pattern on residual stress in selective laser melting, *Int. J. Mach. Tools Manuf.* 145 (July) (2019) 103433.
 - [35] R.J. Williams, C.M. Davies, P.A. Hooper, A pragmatic part scale model for residual stress and distortion prediction in powder bed fusion, *Addit. Manuf.* 22 (January) (2018) 416–425.
 - [36] P. Ferro, L. Romanin, F. Berto, Understanding Powder Bed Fusion Phenomena via Numerical Simulation 53 (2020), pp. 252–284.
 - [37] Q. Chen, et al., An inherent strain based multiscale modeling framework for simulating part-scale residual deformation for direct metal laser sintering, *Addit. Manuf.* 28 (May) (2019) 406–418.
 - [38] P. Prabhakar, W.J. Sames, R. Dehoff, S.S. Babu, Computational modeling of residual stress formation during the electron beam melting process for Inconel 718, *Addit. Manuf.* 7 (2015) 83–91.
 - [39] W. Zhang, M. Tong, N.M. Harrison, Resolution, energy and time dependency on layer scaling in finite element modelling of laser beam powder bed fusion additive manufacturing, *Addit. Manuf.* 28 (2019) 610–620.
 - [40] C. Li, J.F. Liu, Y.B. Guo, Prediction of residual stress and part distortion in selective laser melting, *Procedia CIRP* 45 (2016) 171–174.
 - [41] 3Shape Dental System™, 3Shape, Copenhagen, 2012.
 - [42] E. Savio, L. De Chiffre, R. Schmitt, Metrology of freeform shaped parts, *CIRP Ann. Manuf. Technol.* 56 (2) (2007) 810–835.
 - [43] P.I. Stavroulakis, R.K. Leach, Invited Review Article: Review of Post-Process Optical Form Metrology for Industrial-Grade Metal Additive Manufactured Parts vol. 041101, (2016).
 - [44] R.K. Leach, D. Bourell, S. Carmignato, A. Donmez, N. Senin, W. Dewulf, CIRP annals - manufacturing technology geometrical metrology for metal additive manufacturing, *CIRP Ann. Manuf. Technol.* 68 (2) (2019) 677–700.
 - [45] D.J. Whitehouse, Handbook of Surface and Nanometrology, CRC press, 2010.
 - [46] M. Bayat, S. Mohanty, J. Hattel, Numerical modelling and parametric study of grain morphology and resultant mechanical properties from selective laser melting process of Ti6Al4V, eu spen's 18 th International Conference & 1 (2018) June.
 - [47] C.C. Tutum, J.H. Hattel, Optimisation of process parameters in friction stir welding based on residual stress analysis: a feasibility study, *Sci. Technol. Weld. Join.* 15 (5) (2010) 369–377.
 - [48] E.R. Denlinger, J.C. Heigel, P. Michaleris, Residual stress and distortion modeling of electron beam direct manufacturing, *Eng. Part B: J. Eng. Manuf.* 229 (10) (2015) 1803–1813.
 - [49] F. Richter, Die physikalischen Eigenschaften der beiden Titan-Werkstoffe Ti99.7 und TiAl6V4, *Metall* 42 (1988) 572–575.
 - [50] W. Yan, et al., Meso-scale modeling of multiple-layer fabrication process in Selective Electron beam Melting: Inter-layer/track voids formation, *Mater. Des.* 141 (2018) 210–219.
 - [51] S. Bontha, N.W. Klingbeil, P.A. Kobryn, H.L. Fraser, Effects of process variables and size-scale on solidification microstructure in beam-based fabrication of bulky 3D structures, *Mater. Sci. Eng. A* 513–514 (2009) 311–318 C.
 - [52] M. Chiumenti, et al., Numerical modelling and experimental validation in Selective Laser Melting, *Addit. Manuf.* 18 (2017) 171–185.
 - [53] A.S. Wu, D.W. Brown, M. Kumar, G.F. Gallegos, W.E. King, An experimental investigation into additive manufacturing-induced residual stresses in 316L stainless steel, *Metall. Mater. Trans. A Phys. Metall. Mater. Sci.* 45 (13) (2014) 6260–6270.
 - [54] T. Simson, A. Emmel, A. Dwars, J. Böhm, Residual stress measurements on AISI 316L samples manufactured by selective laser melting, *Addit. Manuf.* 17 (2017) 183–189.
 - [55] X. Lu, et al., Residual stress and distortion of rectangular and S-shaped Ti-6Al-4V parts by Directed Energy Deposition: modelling and experimental calibration, *Addit. Manuf.* 26 (August) (2019) 166–179 2018.
 - [56] M.V. Deo, P. Michaleris, Mitigation of welding induced buckling distortion using transient thermal tensioning, *Sci. Technol. Weld. Join.* 8 (1) (2003) 49–54.
 - [57] T. DebRoy, et al., Additive manufacturing of metallic components – process, structure and properties, *Prog. Mater. Sci.* 92 (2018) 112–224.
 - [58] D. Munro, C. Ayas, M. Langelaar, F. Van Keulen, On process-step parallel computability and linear superposition of mechanical responses in additive manufacturing process simulation, *Addit. Manuf.* 28 (June) (2019) 738–749.